

# Observation of Brane Parity Order in Programmable Optical Lattices

David Wei<sup>1,2</sup>, Daniel Adler<sup>1,2</sup>, Kritsana Srakaew<sup>1,2</sup>, Suchita Agrawal<sup>1,2</sup>, Pascal Weckesser<sup>1,2</sup>,  
Immanuel Bloch<sup>1,2,3</sup> and Johannes Zeiher<sup>1,2</sup>

<sup>1</sup>Max-Planck-Institut für Quantenoptik, 85748 Garching, Germany

<sup>2</sup>Munich Center for Quantum Science and Technology (MCQST), 80799 Munich, Germany

<sup>3</sup>Fakultät für Physik, Ludwig-Maximilians-Universität, 80799 Munich, Germany



(Received 30 January 2023; accepted 2 June 2023; published 29 June 2023)

The Mott-insulating phase of the two-dimensional (2D) Bose-Hubbard model is expected to be characterized by a nonlocal brane parity order. Parity order captures the presence of microscopic particle-hole fluctuations and entanglement, whose properties depend on the underlying lattice geometry. We realize 2D Bose-Hubbard models in dynamically tunable lattice geometries, using neutral atoms in a passively phase-stable tunable optical lattice in combination with programmable site-blocking potentials. We benchmark the performance of our system by single-particle quantum walks in the square, triangular, kagome, and Lieb lattices. In the strongly correlated regime, we microscopically characterize the geometry dependence of the quantum fluctuations and experimentally validate brane parity as a proxy for the nonlocal order parameter signaling the superfluid-to-Mott-insulating phase transition.

DOI: [10.1103/PhysRevX.13.021042](https://doi.org/10.1103/PhysRevX.13.021042)

Subject Areas: Atomic and Molecular Physics

## I. INTRODUCTION

According to seminal work by Landau, second-order phase transitions are signaled by a change of a local order parameter. However, some phase transitions defy this classification in terms of a local order parameter and require, as a generalization, nonlocal order parameters to describe their underlying structure [1,2]. The Haldane insulator constitutes a celebrated example for such a phase, in which a string correlator captures the underlying nonlocal hidden order [3,4], which has also recently been realized experimentally [5,6]. Interestingly, the Mott-insulating (MI) phase of the Bose-Hubbard (BH) model also features nonlocal order, which accounts for quantum fluctuations in the form of bound particle-hole pairs [7–9]. In one-dimensional (1D) BH chains, the MI order has been revealed by a parity order parameter of the on-site occupation [7,8,10]. In two dimensions (2D), brane parity was proposed as a generalization of parity order for square lattices [11,12]. However, up to now, experiments directly measuring brane parity in any 2D lattice geometry are lacking, as well as its experimental validation as an order parameter for the MI phase in 2D. A strategy to achieve the latter is provided by mean-field theory, which predicts that the location of the

phase transition should scale with the coordination number and thus the underlying lattice geometry. This scaling was explicitly probed by measuring the local order parameter in the superfluid (SF) phase [13]. Observing such scaling also in brane parity provides an indication for the suitability of brane parity as a 2D nonlocal order parameter.

Neutral atoms in optical lattices provide a pristine test bed to realize low-dimensional Hubbard models [14] and offer techniques for the detection of local observables using quantum gas microscopes [15,16]. Optical lattices arise through the interference pattern of laser beams, whose layout is carefully chosen for a specific target geometry and has led to the realization of a variety of lattices [17–21]. While optical lattices benefit from their inherent homogeneity and stability, the static nature of a given beam layout restricts systems to fixed spatial geometries and makes dynamical changes within a single experimental run challenging. In contrast, arrays of optical tweezers can be generated in almost freely programmable geometries [22] and have allowed for studies of a variety of many-body spin models. A number of approaches have been brought forward to allow for similar programmability for itinerant atoms based on realizing small systems of tunnel-coupled optical tweezers [23,24] or dynamically controllable lattices [17]. However, tweezer arrays in the itinerant regime are difficult to scale to large system sizes due to inhomogeneities and, concomitantly, a large calibration overhead. The realization of dynamically controlled lattices—pioneered in Ref. [17] to explore topological band structures and subsequently applied in several experiments [25–27]—typically involves active phase stabilization techniques,

Published by the American Physical Society under the terms of the [Creative Commons Attribution 4.0 International](https://creativecommons.org/licenses/by/4.0/) license. Further distribution of this work must maintain attribution to the author(s) and the published article's title, journal citation, and DOI. Open access publication funded by the Max Planck Society.

which come with experimental overhead to guarantee reliable operation.

Here, we report on the realization of 2D Bose-Hubbard models in passively phase-stable optical lattices with square or triangular base geometry, which we combine with local site-blocking beams to realize programmable unit cells. We demonstrate this novel degree of flexible control by implementing square, triangular, kagome, and Lieb lattices in one experimental setup and benchmark their quality through single-particle quantum walks. Increasing the atomic density, we microscopically probe the strongly interacting regime through nonlocal quantum fluctuations and show their dependence on the underlying lattice structure. Our measurements provide a quantitative characterization of the phase transition point in these lattices and experimentally establish brane parity [8,11,12] as a meaningful nonlocal observable to characterize the SF-MI phase transition in 2D models.

## II. PROGRAMMABLE LATTICES

In our approach to realizing tunable lattice geometries, we superpose a bow-tie lattice [28] (L2) with a mutually noninterfering retroreflected 1D lattice (L1); see Fig. 1(a). The two lattices are not only intrinsically phase stable but also relative to each other as they are both phase referenced to a common retroreflection mirror (see Appendix A). The relative phase between the lattice potential minima, which we refer to as “superlattice phase”  $\Delta\varphi$ , can be adjusted by introducing a slight detuning between the lattice frequencies (taking into account the distance between atoms and the retroreflecting mirror). By additionally varying the power ratio between the lattice beams  $V_1/V_2$ , the ground band behavior can be tuned between square, triangular, honeycomb, and 1D lattices. This setup realizes the flexibly tunable lattice potential introduced in Ref. [17] while avoiding the need for auxiliary beams or lattice phase modulation required for active phase locking. On top of these base lattices, we employ a digital micromirror device (DMD) to project single-site-resolved beams through the microscope objective; see Fig. 1(f). This procedure results in a programmable repulsive potential landscape, blocking atomic occupation on specific lattice sites, which allows for the realization of an even larger class of derived lattice potentials; see Figs. 1(d) and 1(e). At the same time, with light only applied to blocked-out sites, this scheme minimizes cross-talk, reducing undesired local disorder. The phase stability between these microscopic blocking beams and the base lattice is ensured by active feed forward to correct for slow thermal drifts [29].

## III. LATTICE CHARACTERIZATION

In our experiment, we work with about 200  $^{87}\text{Rb}$  atoms in the  $|F = 1, m_F = -1\rangle$  ground state, trapped in lattices at a wavelength of  $\lambda = 1064$  nm and with DMD block-out

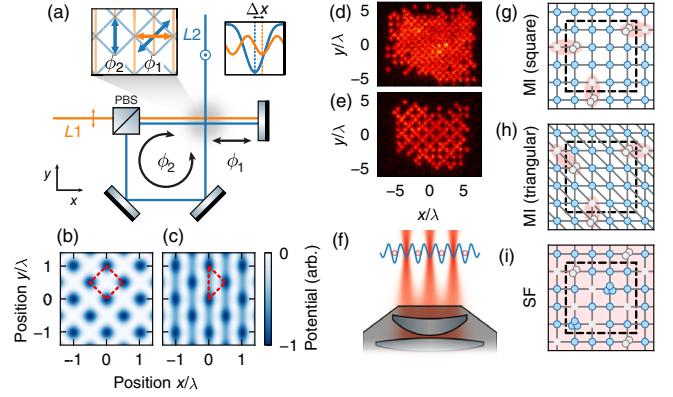


FIG. 1. (a) Experimental setup realizing passively phase-stable tunable lattices. The lattice 2 beam (L2, blue) is out-of-plane polarized and forms a bow-tie lattice, realizing a square lattice potential (b). The in-plane polarized lattice 1 beam (L1, orange) can be added, with a well-defined superlattice phase  $\Delta\varphi = 2\pi\Delta x/(\lambda/2)$  (see lattice potentials sketched in the right inset). For the in-phase case,  $\Delta\varphi = 0$ , an effective triangular lattice geometry is realized (c). In the left inset, the combined lattice is passively phase stable due to the retroreflection mirror serving as a common phase reference. Temporal fluctuations of path lengths lead to translations along either common paths or along translationally invariant directions. The arrows indicate the movement of the interference pattern generated by the respective lattice upon changes in the phase  $\phi_{1,2}$ . (d),(e) Single-site resolved image of a Mott insulator in the square (d) and Lieb lattice (e). (f) Lattices with more complex unit cells, e.g., as shown in panel (e), which can be dynamically generated by projecting repulsive local potentials through the objective, blocking out distinct lattice sites. (g)–(i) MI phase hosting doublon-hole pairs (red shading), observable as correlated parities (blue: positive; gray: negative). Brane parity serves as a proxy for a nonlocal order parameter and is given by the product of the on-site parities evaluated over an analysis area (black frame). In the MI phase (g),(h), its value is positive (for finite areas) and depends on the number of doublon-hole pairs cut by the analysis boundary. In the SF phase (i), parities are nearly uncorrelated, leading to a substantially smaller brane parity.

beams operating at 670 nm. For the data presented here, we optimize the superlattice phase for the triangular lattice condition  $\Delta\varphi = 0$  and extract a phase stability of  $\sigma_{\Delta\varphi} = 0.01(1)\pi$  using L1 amplitude modulation spectroscopy (see Appendix A). Starting with a 2D superfluid trapped in a single layer of a vertical 1D lattice, we adiabatically ramp up the horizontal lattices (L2, L1), such that the atoms form a unity-filled Mott insulator with a typical filling of 0.97. After performing measurements in the desired lattice configuration, we ramp off L1 and perform single-site resolved fluorescence imaging in L2. Because of pairwise losses during fluorescence imaging, the resulting single-shot images reveal the local atom number parity [16].

To demonstrate the flexible control over the lattice geometry and benchmark the corresponding properties of the ground band, we perform single-particle quantum

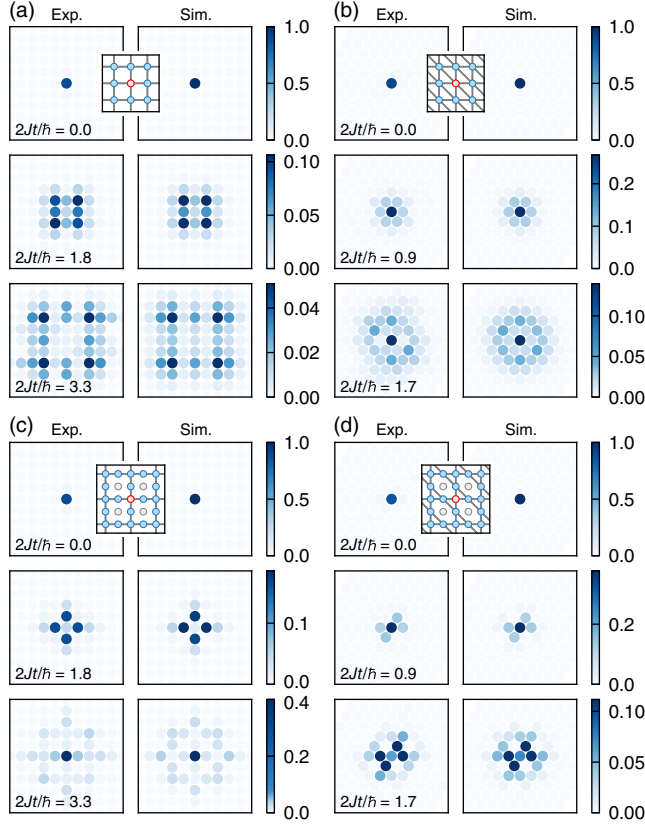


FIG. 2. Atomic densities due to quantum walks in various lattice geometries. After preparing a single localized atom in the center of the lattice (red site in insets), we measure the ballistic dynamics of the wave function at various times (top to bottom). The square (a) and triangular (b) lattices are realized in the ground band of our superlattice. The Lieb (c) and kagome (d) lattices are generated by locally projecting repulsive light on certain sites (gray sites in insets). The interference fringes visible in the experimental data (left) agree well with simulations (right), indicating coherent evolution in a homogeneous and stable lattice. Note that some color-map ranges have been adjusted to facilitate displaying the large dynamic range.

walks [30–32] in the respective 2D lattices. To achieve this goal, we flip the hyperfine state of a single atom using our local microwave addressing technique based on a DMD [29,30]. After pushing out all but the spin-flipped atom, we quench the lattices to a depth where the particle is allowed to tunnel. As the wave function spreads coherently, we expect the evolving site-resolved probability distribution to display interference patterns characteristic of the specific lattice.

The density dynamics averaged over 250 experimental repetitions and their hopping symmetry axes is displayed in Fig. 2, showing excellent agreement with simulations. In the square lattice at  $10.0(3)E_r^{(752)}$  depth, where  $E_r^{(a/nm)} = \hbar^2/8ma^2$  denotes the recoil energy of the respective lattice with spacing  $a$ , the two dimensions decouple, and we observe the characteristic ballistically expanding wavefront

with a fitted hopping energy of  $J = \hbar \times 31(1)$  Hz along the horizontal and  $J_v = 0.92(1)J$  along the vertical direction; see Fig. 2(a). This agrees well with the hopping rates obtained from band-structure calculations using the lattice depth independently calibrated by amplitude modulation spectroscopy. The small observed anisotropy is well reproduced in our simulations when considering the difference in the lattice spacings as L2 intersects slightly non-orthogonally at an angle of  $90.7(1)^\circ$ . For the triangular lattice, the depths are tuned to an isotropic coupling ratio, following the relation  $V_1/E_r^{(532)} \approx 4 + V_2/E_r^{(752)}$ . The associated quantum walk measurements shown in Fig. 2(b) are performed at  $V_2 = 4.0(1)E_r^{(752)}$  with  $J = \hbar \times 21(1)$  Hz and exhibit circularly symmetric expansion with a fitted residual diagonal anisotropy of  $J_d = 1.05(2)J$ . In general, the tunability of the ratio  $V_1/V_2$  enables us to deliberately vary the diagonal anisotropy, interpolating between a square and a 1D lattice along the diagonal (see Appendix B).

To characterize the emergent programmable lattices in the presence of microscopic site-blocking potentials of  $V_b = \hbar \times 300(90)$  Hz, we measure quantum walks at the same base-lattice parameters as above. For the block-out potential presented in Figs. 2(c) and 2(d), the expected lattice geometries are the Lieb and kagome lattices for the square or triangular base lattices, respectively. We again find excellent agreement with simulations and observe that the atom population remains on the nonblocked sites with 99(1)% probability, while cross-talk-induced disorder is small.

#### IV. DOUBLON-HOLE FLUCTUATIONS

After characterizing the single-particle tight-binding bands and the stability of the generated lattices through the quantum walks, we proceed by studying the interacting regime in the unity-filling Bose-Hubbard model realized on the various lattice geometries. While the ground state in the atomic limit ( $J/U \ll 1$ ) corresponds to a unity-filled product state, quantum fluctuations in the form of doublon-hole pairs emerge on top of the product state at finite tunnel couplings [7,9]. In a perturbative picture, regardless of the exact lattice geometry, every bond in an isotropic lattice is expected to give rise to equal nearest-neighbor  $\langle i, j \rangle$  parity correlations of  $C = \langle \hat{s}_i \hat{s}_j \rangle - \langle \hat{s}_i \rangle \langle \hat{s}_j \rangle \approx 16J^2/U^2$ , where  $\hat{s}_j = e^{i\pi\delta\hat{n}_j}$  denotes the local atom number parity, with  $\delta\hat{n} = \hat{n} - 1$  representing the deviation from the mean occupation. In the experiment, we start with a 2D SF and then slowly increase the local block-out potential in 150 ms to  $V_b = \hbar \times 450(120)$  Hz. Subsequently, the horizontal lattices are adiabatically and isotropically increased to a depth corresponding to the desired  $J/U$  parameters in 200 ms, followed by a fast 1-ms ramp to  $V_2 = 90E_r^{(752)}$ , which freezes all quantum fluctuations. The interaction

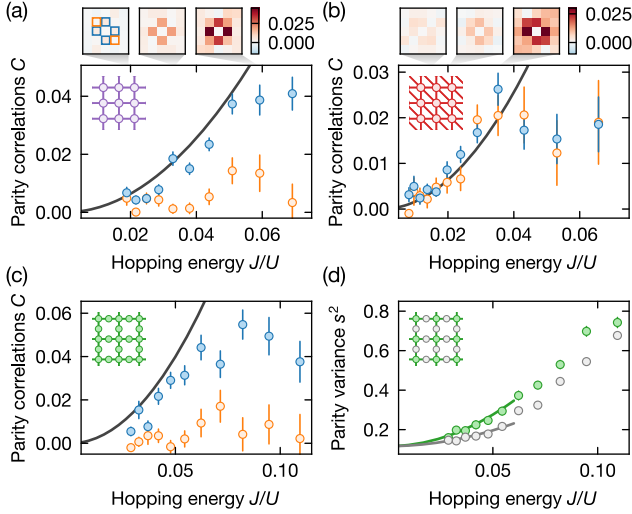


FIG. 3. Doublon-hole fluctuations in the square (a) and the triangular lattice (b). The straight-neighbor parity correlations (blue) grow with  $(J/U)^2$  in both cases (line). The correlations of the diagonal neighbor (orange), however, only grow in the case of the triangular lattice. The color plots (top) show the 2D parity correlations  $C$  of the neighboring sites. The colored edges in the leftmost plot indicate the value shown in the main plot. (c) Fluctuations in the Lieb lattice averaged over both hub and rim sites, showing a behavior similar to the square lattice case in the perturbative regime  $J \ll U$ . The insets in panels (a)–(c) depict the lattice geometry. (d) Fluctuations driven by coupling to neighboring sites and thus the local coordination number. The coordination number of the Lieb lattice depends on the site within the unit cell. Accordingly, the on-site variance on the hub sites (green) grows twice as fast as the rim sites (gray); see inset. Solid lines show perturbative calculations, with an offset that accounts for the finite filling of 0.97. Error bars denote the standard deviation (s.d.) from a bootstrap analysis.

energies in this measurement are in the range of  $U = h \times 200\text{--}300$  Hz. In Figs. 3(a)–3(c), we compare the correlations from 200 experimental runs evaluated over  $9 \times 9$  sites along the straight and diagonal neighbors for the square, triangular, and Lieb lattices. We clearly observe that diagonal correlations only arise in the case of the triangular lattice. Furthermore, the growth in correlations agrees with the perturbative dependence within its range of validity for all lattice geometries along their respective bond directions. When approaching the phase transition, the pairs rapidly deconfine, resulting in the observed reduction of neighboring correlations [7]. Our presented data are subject to less than 10% of deviations in the hopping energies due to hopping anisotropies and lattice calibration, and we estimate about a 6% reduced correlator strength due to finite temperatures.

In the case of the tripartite Lieb lattice, there exist two types of sublattices with differing local coordination number  $z$ : the hub sites with  $z = 4$  and the rim sites with  $z = 2$ . This geometry gives rise to a flat central band,

whose Bloch wave functions exclusively populate the rim sites [33], which suggests that the influence of the flat band might manifest as spatially distinct behavior on the two sublattice types. In particular, in the SF phase, the superfluid density is expected to be higher on the hub sites [34,35] and may be viewed as a tendency to depopulate the flat band. To capture the effects of this spatial inhomogeneity, we analyze the on-site variance  $s^2 = \langle \hat{s}_j^2 \rangle - \langle \hat{s}_j \rangle^2$  averaged over either sublattice type; see Fig. 3(d). We can indeed observe that the variance differs between the two types of sites when approaching the phase transition, with the hub sites displaying higher fluctuations. In the MI phase, the on-site fluctuations correspond to the formation of doublon-hole pairs with the site's  $z$  neighbors, and they grow with  $J/U$  as described by perturbation theory. In the SF phase, we would similarly expect the sublattices to show distinct atom number fluctuations due to the inhomogeneous superfluid density. However, as the parity is bounded, the parity variance is also bounded, and at large  $J/U$ , the difference in the parity variance decreases again.

## V. BRANE PARITY

The different nature of the occupation fluctuations in the SF and MI phases can furthermore be used to construct a nonlocal order parameter characterizing the Mott-insulating phase: The brane parity order parameter is given by the product of all parities as

$$\hat{O}_P = \prod_{i \in L \times L} \hat{s}_i^{1/\Lambda} = e^{i\pi \delta \hat{N} / \Lambda}, \quad (1)$$

where  $1/\Lambda$  parametrizes the generally fractional parity,  $e^{i\pi \delta \hat{n}_i / \Lambda}$ , and  $\delta \hat{N} = \sum_{i \in L \times L} \delta \hat{n}_i$  denotes the total atom number deviation within a region of interest (ROI),  $L \times L$ . In the Mott-insulating phase, fluctuations in the occupation remain local, as shown above via the doublon-hole correlations. Hence, fluctuations inside the ROI leave the atom number invariant, resulting in an  $\hat{O}_P$  value of unity. However, when the edge of the ROI cuts a doublon-hole pair [see Figs. 1(g) and 1(h)], the atom number within the ROI changes, resulting in a reduced  $\hat{O}_P$ . In contrast, fluctuations in the superfluid phase are global [see Fig. 1(i)], such that *any* fluctuation leads to changes in the atom number within the ROI. This difference demonstrates that  $O_P$  can quantify the nonlocal nature of a given state and give rise to distinct  $L$ -scaling behavior, which can be approximated as  $\log O_P \sim -L/\Lambda^2$  in the MI and  $\log O_P \sim -(L \log L)/\Lambda^2$  in the SF, respectively [8,12]. In the thermodynamic limit, brane parity serves as a true order parameter for fractional parities with  $1/\Lambda = 1/\sqrt{L}$  [12] as it remains finite in the MI phase while vanishing in the SF phase [11,12]. As our experimental setup gives access to only the integer parities  $\hat{s}_i$  instead of the full occupation  $\hat{n}_i$ , we focus on integer brane parity,  $\Lambda = 1$ ,

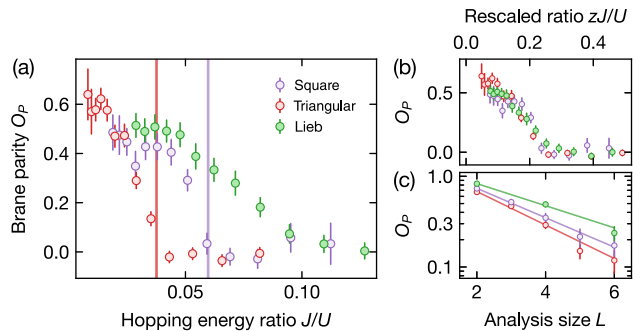


FIG. 4. (a) Brane parity across the SF-MI phase transition for various lattice geometries analyzed over  $4 \times 4$  sites. The measurements in the triangular (red), square (purple), and Lieb (green) lattices all show a change from zero to finite values of integer brane parity. The critical  $(J/U)_c$  agrees with the phase transition point obtained from quantum Monte Carlo simulations (solid lines), indicating its suitability as a nonlocal order parameter for the Mott-insulating phase. (b) Rescaling the hopping energy with the respective (averaged) coordination number  $z$  of the lattice, we find a collapse of the data, showing that the phase transition scales with  $z$ . (c) Dependence of integer brane parity with the analysis area containing  $L \times L$  sites in the MI phase at  $J/U = 0.029$  (triangular, red),  $0.029$  (square, purple), and  $0.033$  (Lieb, green). Solid lines denote an exponential fit consistent with perimeter-law scaling. The Lieb lattice only contains even data points due to its  $2 \times 2$ -site unit cell. Error bars denote the s.d. from a bootstrap analysis.

which is expected to yield a perimeter-law decay of  $\log O_P \sim -L$  in the MI phase. However, as  $O_P$  remains finite for any *finite* analysis area and has a parametrically larger absolute value in the MI than in the SF phase, integer brane parity is still useful as a proxy for the true MI order parameter and can capture the critical  $(J/U)_c$  within experimental uncertainties (see Appendix C).

In Fig. 4(a), we plot integer brane parity evaluated over a  $4 \times 4$  area as a function of  $J/U$  for the triangular, square, and Lieb lattices. For data in the MI phase, varying the analysis area furthermore shows scaling consistent with a perimeter law; see Fig. 4(c). In all geometries, the location of the phase transition is clearly represented as a departure of brane parity from zero. The experimentally obtained critical values  $(J/U)_c \approx 0.04$  and  $0.06$  for the triangular and square lattices, respectively, agree well with quantum Monte Carlo simulations [36,37]. We furthermore find a collapse of  $O_P$  for the different lattices when rescaling the hopping energy with the coordination number of the lattice; see Fig. 4(b). The observed collapse is consistent with predictions by mean field theory and measurements of the superfluid order parameter [13], thus providing further validation for the use of brane parity as a proxy for the nonlocal order parameter. Interestingly, we also observe the collapse for the Lieb lattice when using the arithmetic mean of its local constituents as an effective coordination number. The systematic deviations for the Lieb lattice towards

higher parity values near the phase transition could hint at a stabilizing effect of the flat band on the MI phase, which is not captured by the applied simple rescaling with coordination number—a point that needs further investigation by theory and experiment.

## VI. CONCLUSION

Employing a quantum gas microscope, we have demonstrated a passively phase-stable approach to realizing 2D Hubbard systems in programmable lattice geometries. In various lattices, our microscopic measurements have experimentally established integer brane parity as a nonlocal observable suitable to characterize the 2D SF-MI phase transition. Dimerizing sites with an out-of-phase superlattice to separate doublons into distinct sites, followed by site-resolved imaging in the honeycomb lattice, would furthermore allow for distinguishing doublons from holes [17,25], which could enable the detection of the fractional parity order for both bosonic and fermionic systems [11,12]. Finally, our microscopic programmability of on-site potentials enables the exploration of further lattice-dependent many-body phenomena, ranging from the engineering of novel Hamiltonians on top of flat bands hosting exotic phases [33,38] to studying transport through interfaces between regions with differing lattice geometry.

## ACKNOWLEDGMENTS

We thank Jae-yoon Choi and Dan Stamper-Kurn for valuable discussions. We acknowledge funding by the Max Planck Society (MPG), the European Union (PASQuanS Grant No. 817482), and the Deutsche Forschungsgemeinschaft (DFG, German Research Foundation) under Germany’s Excellence Strategy–EXC-2111–390814868. K. S. and S. A. acknowledge funding from the International Max Planck Research School (IMPRS) for Quantum Science and Technology.

*Note added.*—Recently, we became aware of related work microscopically studying fermionic many-body systems in actively phase-stabilized tunable lattice geometries [27] and measuring brane parity order with error-corrected snapshots [39].

## APPENDIX A: LATTICE PROPERTIES

### 1. Lattice phase stability

In the tunable base lattices implemented in Refs. [17,27], where two independent but mutually interfering retro-reflected laser beams are crossed, active phase stabilization is required due to the “time phase” difference between the two beams,  $\alpha$ , being an unrestricted degree of freedom. For beams with wave number  $k = 2\pi/\lambda$  with a combined field given by  $A \sim e^{iky} + e^{-iky} + e^{i\alpha}e^{ikx} + e^{i\alpha}e^{-ikx}$ , the intensity becomes  $|A|^2 \propto \cos 2x + \cos 2y + 4 \cos \alpha \cos x \cos y$  and

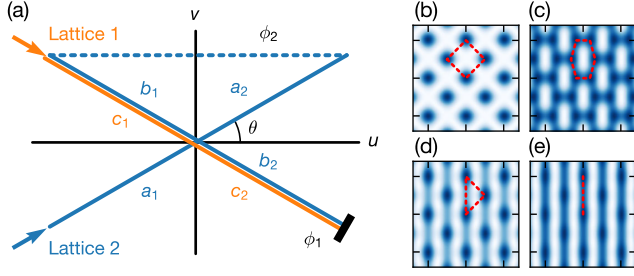


FIG. 5. (a) Lattice beam layout denoting intersection half-angle  $\theta$ , field amplitudes of the incident beam passes  $\{a_i, b_i, c_i\}$ , and phase delays  $\{\phi_i\}$  introduced by propagation. The superlattice phase  $\Delta\varphi$  is depicted in Fig. 6(a). At an intersection angle of  $2\theta = 90^\circ$ , various lattice geometries can be realized [17] as follows: in the absence of lattice 1, a square lattice (b); in its presence, a honeycomb lattice for  $\Delta\varphi = \pi$  (c); a triangular lattice for  $\Delta\varphi = 0$  (d); and a 1D lattice in the limit of deep lattice 1 (e).

thus realizes an interference structure that depends on  $\alpha$ . As bow-tie lattices (as used in our setup) fold the same beam into the orthogonal axis, the time phase difference is inherently fixed to  $\alpha = 0$ . In the following, we furthermore show that this lattice is also structurally phase stable with respect to variations in the “spatial phases” when superposing with an additional 1D lattice.

The layout of our lattice beams is shown in Fig. 5, with the two axes  $\mathbf{k}_{x,y} = k(\cos\theta, \mp \sin\theta)$ . The square lattice generated by lattice 2 and the 1D lattice generated by lattice 1 have respective fields of  $A_2 = a_1 e^{i(\mathbf{k}_y \cdot \mathbf{r})} + b_1 e^{i(\mathbf{k}_x \cdot \mathbf{r} + \phi_2)} + b_2 e^{i(-\mathbf{k}_x \cdot \mathbf{r} + \phi_2 + 2\phi_1)} + a_2 e^{i(-\mathbf{k}_y \cdot \mathbf{r} + 2\phi_2 + 2\phi_1)}$  and  $A_1 = c_1 e^{i(\mathbf{k}_x \cdot \mathbf{r})} + c_2 e^{i(-\mathbf{k}_x \cdot \mathbf{r} + 2\phi_1 + \Delta\varphi)}$ , where  $\Delta\varphi$  indicates the superlattice phase. This yields an overall light intensity of

$$\begin{aligned} I &= |A_1|^2 + |A_2|^2 \\ &= (a_1^2 + a_2^2 + b_1^2 + b_2^2 + c_1^2 + c_2^2) \\ &\quad + 2c_1 c_2 \cos[2k(u - u_0) \cos\theta - 2k(v - v_0) \sin\theta - \Delta\varphi] \\ &\quad + 2a_1 a_2 \cos[2k(u - u_0) \cos\theta + 2k(v - v_0) \sin\theta] \\ &\quad + 2b_1 b_2 \cos[2k(u - u_0) \cos\theta - 2k(v - v_0) \sin\theta] \\ &\quad + 2(a_1 b_1 + a_2 b_2) \cos[2k(v - v_0) \sin\theta] \\ &\quad + 2(a_1 b_2 + a_2 b_1) \cos[2k(u - u_0) \cos\theta], \end{aligned} \quad (\text{A1})$$

where we have defined  $2ku_0 \cos\theta = \phi_2 + 2\phi_1$  and  $2kv_0 \sin\theta = \phi_2$ . Thus, the lattice potential only depends on a translated position  $(u - u_0, v - v_0)$ , confirming that, structurally, the lattice is passively phase stable. The potential structure corresponds to the one realized in Ref. [17] but is subject to an additional  $\phi_1$ -induced translational phase shift along the lattice 2 axis due to the folded layout.

## 2. Bose-Hubbard parameters

The Bose-Hubbard model is given by

$$\hat{H} = -\sum_{\langle i,j \rangle} J_{ij} \hat{c}_i^\dagger \hat{c}_j + \frac{U}{2} \sum_i \hat{n}_i (\hat{n}_i - 1) + \sum_i V_i \hat{n}_i. \quad (\text{A2})$$

The on-site potential  $V_i$  is experimentally calibrated, as described in Appendix C. The hopping energy  $J_{ij}$  and interaction energy  $U$  are theoretically calculated and verified for certain values by fitting the quantum walk measurements and modulation spectroscopy, respectively. Since the lattice potential  $V(u, v) \propto -I(u, v)$  is not separable, we perform a full 2D band-structure calculation following Ref. [40]. On the one hand, this calculation yields the band gaps used for the lattice depth calibration (see Appendix B). On the other hand, we obtain the ground-state Wannier wave functions  $w_j(u, v)$  on lattice site  $j$ , which we use to determine the hopping energy between sites  $i$  and  $j$  by evaluating

$$J_{ij} = \int du dv w_i^*(u, v) \left( -\frac{\hbar^2}{2m} \nabla^2 + V(u, v) \right) w_j(u, v)$$

and the Hubbard interaction energy

$$U = \frac{4\pi\hbar^2 a_s}{m} \int du dv dz |w(u, v) w^z(z)|^4$$

where  $a_s$  is the  $s$ -wave scattering length. The Wannier function for the vertical direction  $w^z(z)$  is independently obtained from a 1D band-structure calculation due to the separability of the lattice potential along this direction.

For the lattice geometries with site block-out, we consider the influence of the block-out potentials within the tight-binding model since the band gaps, which are greater than  $h \times 3$  kHz, are much larger than the block-out potentials, which are less than  $h \times 450$  Hz.

## APPENDIX B: SINGLE-PARTICLE MEASUREMENTS

### 1. Modulation spectroscopy

We calibrate the individual lattice depths by performing amplitude modulation spectroscopy and find two  $d$ -band resonances from which we determine the lattice depth with about 2% uncertainty.

For the superlattice phase measurements shown in Fig. 6, we amplitude-modulate lattice 1 within a deep lattice-2 potential near the upper  $p$ -band resonance. Because of the weak single-particle drive in an isolated system, we analyze the response assuming a two-level model with coupling  $\Omega$  and modulation-frequency detuning  $\Delta$ . This model yields a mean excited-state population of  $P_e(\Omega, \Delta) = 2/(4 + \delta^2 + \sqrt{\delta^2(4 + \delta^2)})$ , with  $\delta = \Delta/\Omega$ . Close to the superlattice in-phase condition,  $\Delta\varphi = 0$ , the

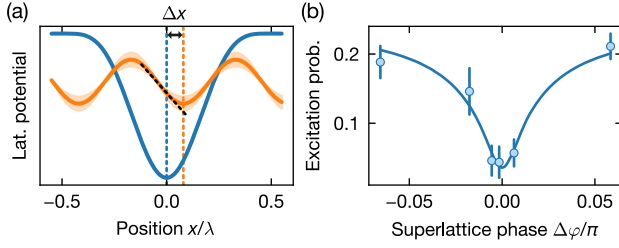


FIG. 6. (a) The superlattice phase,  $\Delta\varphi = 2\pi\Delta x/(\lambda/2)$ , can be precisely calibrated by amplitude-modulating lattice 1 (orange solid line) near the band-gap frequency of a much deeper lattice 2 (blue solid line). Single-band excitations require dipolar modulation (black dashed line), which is minimal when the lattices are in phase ( $\Delta\varphi = 0$ ). The vertical dashed lines represent the potential minima (and thus phase) of the respective lattices. (b) Single-band amplitude modulation spectroscopy probing the resonant-band excitation probability at the respective superlattice phase. The solid line shows a fit from which we extract a superlattice phase stability of  $\sigma_{\Delta\varphi} = 0.01(1)\pi$ , which was confirmed in a long-time measurement. Error bars denote the standard error of the mean (SEM).

coupling is proportional to the superlattice phase (here,  $\Omega/\Delta\varphi \approx 660 \text{ Hz h}/\pi$ ), which we calculate from the band-structure results. Considering the long and weak drives, we assume that Gaussian fluctuations in the superlattice phase ( $\propto \sigma_{\Omega}$ ) and in the lattice depth ( $\propto \sigma_{\Delta}$ ) dominate the shape of the resonance. Thus, the excitation probability on resonance is given by the twofold convolution over the fluctuations, yielding

$$\bar{P}_e(\Omega) \sim 1 - \int f_{\mathcal{N}(\omega, \sigma^2)}(x) e^{x^2} \text{erfc}|x| dx, \quad (\text{B1})$$

where  $\text{erfc}$  denotes the complementary error function, and  $f_{\mathcal{N}(\omega, \sigma^2)}$  is the probability of a normal distribution with center  $\omega^2 = 2\Omega^2/\sigma_{\Omega}^2$  and variance  $\sigma^2 = \sigma_{\Omega}^2/2\sigma_{\Delta}^2$ .

In the experiment, we tune the superlattice phase by varying the frequency difference  $\Delta f$  between the lattices using an acousto-optic modulator, which yields a tuning slope of  $\Delta\varphi/\Delta f \approx \pi/250 \text{ MHz}$  for the distance between atoms and retroreflecting mirror of about 300 mm. At a lattice-2 depth of  $V_2 = 185(5)E_r^{(752)}$ , where all dynamics in the lattice are frozen and where we can separate the lattice into its local potential wells, we modulate lattice 1 at  $V_1 = 5.0(2)E_r^{(532)}$ , with a modulation depth of 0.25. As a spectroscopic signature, we measure the fraction of atoms remaining in the ground band after modulation by adiabatically lowering the lattice depth to  $V_2 \approx 18E_r^{(752)}$ , leading to the loss of atoms populating higher bands; see Fig. 6(b). By fitting the functional shape of Eq. (B1) to our experimental data and converting from coupling strength to the superlattice phase, this model allows us to extract a standard deviation of the superlattice phase of  $\sigma_{\Delta\varphi} = 0.01(1)\pi$ . Repeating this measurement weeks later

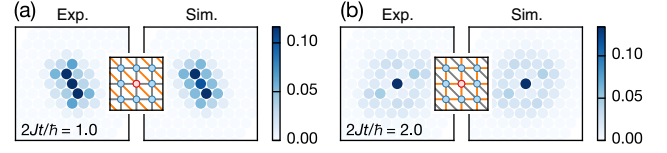


FIG. 7. Densities due to quantum walks in anisotropic triangular lattices with fitted hopping energy ratios between diagonal and horizontal neighbors of  $J_d/J = 1.69(3)$  (a) and  $0.79(2)$  (b). The insets show the site connectivity, with stronger couplings highlighted in orange.

gave a similar excitation probability, demonstrating the long-term stability of this lattice scheme.

## 2. Quantum walks

The quantum walk measurements shown in Fig. 2 are performed by preparing a single atom and lowering the lattice-2 depth from  $25E_r^{(752)}$  (for square geometries) and  $15E_r^{(752)}$  (for triangular geometries) to the depth used for the dynamics measurements in 2.5 ms to avoid band excitations. After the time evolution, we freeze the dynamics by ramping up lattice 2 to  $25E_r^{(752)}$  in 0.8 ms. We postselect the data for a single detected atom and fit the resulting time-dependent densities to numerical simulations of the respective tight-binding lattice. For the base lattice geometries, we fit the hopping energy along each bond direction, as well as a time offset  $t_0$  to account for the finite ramp times, yielding  $2Jt_0 = 0.60(1)$  and  $0.32(5)$  for the square and triangular geometries, respectively. The parameters of the base lattice fits are used for the Lieb and kagome lattice simulations and agree with a direct fit to the data.

By varying the depth ratio  $V_1/V_2$  between the lattices, we can furthermore tune the hopping energy ratio between the straight bonds and the diagonal bonds, i.e., the geometry between a square lattice for  $V_1 \ll V_2$  and a 1D lattice for  $V_1 \gg V_2$ . In Fig. 7, we show quantum walks, in analogy to Fig. 2, performed with intermediate anisotropic hopping ratios, which similarly agree with simulations.

Quantitative comparisons between calibrated and fitted hopping energies are presented in Table I, showing lattice-depth-dependent anisotropies, with the coupling anisotropies along the straight bonds being well captured by the band-structure calculations. We can further observe deviations of the absolute scales, giving rise to relative uncertainties of up to 10%, which suggest slight imperfections in the lattice beam parameters.

## APPENDIX C: MANY-BODY MEASUREMENTS

### 1. On-site potential calibration

Our vertical lattice creates a spatially inhomogeneous in-plane confinement potential. To estimate its potential depth,

TABLE I. Base lattice hopping energies obtained through fits to the quantum walk measurements and from band-structure calculations using lattice depths calibrated by amplitude-modulation spectroscopy.

Geometry	Lattice	Depth	Axis	Calculations	Fit	
Square	$V_2/E_r^{(752)}$	10.0(3)	$J/h$	32.9(9)	31.2(6)	
			$J_v/h$	30.8(9)	28.8(6)	
Triangular	$V_2/E_r^{(752)}$	3.9(2)	$J/h$	14.1(12)	15.8(3)	
			$V_1/E_r^{(532)}$	$J_v/h$	13.4(12)	15.1(3)
				$J_d/h$	16.3(8)	16.7(3)
Positive	$V_2/E_r^{(752)}$	3.9(2)	$J/h$	9.0(8)	9.0(2)	
anisotropic	$V_1/E_r^{(532)}$	10.4(3)	$J_v/h$	8.6(8)	8.9(2)	
			$J_d/h$	16.1(8)	15.2(3)	
Negative	$V_2/E_r^{(752)}$	3.9(2)	$J/h$	22.5(16)	22.4(5)	
			$V_1/E_r^{(532)}$	$J_v/h$	21.5(16)	22.6(5)
				$J_d/h$	16.4(8)	17.7(4)

we increase the atom number loaded into the system until a doubly filled Mott insulator forms in the center. The outline of the atomic cloud then gives us the equipotential line at a potential depth of the Hubbard interaction energy  $U$ . Because of fluctuations in the atom number, the major source of uncertainty for this calibration method stems from determining the outline of the cloud.

Using this information, we calibrate the projected DMD potential for blocking out the lattice sites. We adiabatically ramp the square lattice into the atomic limit with the projected potential switched on. While keeping the atom number such that the outline of the atomic cloud remains near the  $U$ -equipotential line, we vary the projected light power. When reaching a projected potential of  $U$ , we expect the population on the central blocked-out sites to vanish. We therefore calibrate the DMD potential by mapping the light power where the average filling of the central blocked-out sites reaches less than 0.03 to a potential shift of around  $U$ .

## 2. Lieb sublattice inhomogeneity

In order to validate the observation that the parity variance differs between the hub and rim sublattice sites of the Lieb lattice as shown in Fig. 3(d), we plot the variance difference in Fig. 8. Comparing to the same analysis performed in the square and triangular lattices, we can see that only the Lieb lattice shows a significant deviation from zero.

We expect the sublattice-dependent occupation fluctuations to grow further into the SF phase; however, the data show a peak already around the phase transition point. We attribute this observation to the fact that, in contrast to the atom number, the parity is bounded, which limits the observable fluctuations. This behavior is also qualitatively

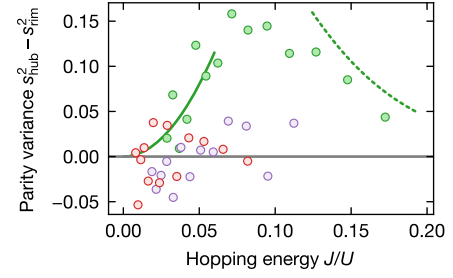


FIG. 8. Parity variance on the hub sites  $s_{\text{hub}}^2$  subtracted by the variance on the rim sites  $s_{\text{rim}}^2$  for the triangular (red), square (purple), and Lieb (green) lattices. The local variance differs significantly only for the Lieb lattice. The solid line indicates perturbative on-site fluctuations from doublon-hole pairs in the MI phase. The dashed line indicates inhomogeneous mean-field calculations at  $\mu/U = 0.5$  in the SF phase.

reproduced by inhomogeneous mean field calculations [34], which similarly show a reduction in the parity variance difference with increasing  $J/U$ .

## 3. Finite-size scaling of integer brane parity

To maximize the signal-to-noise ratio of integer brane parity extracted from experimental data, we first crop the images to a  $7 \times 7$ -site area in the center of the atomic cloud. We then evaluate brane parity for all possible  $L \times L$ -site analysis areas within the original  $7 \times 7$  sites and average over the results. Note that in the case of the Lieb lattice, we flip the sign of  $O_p$  for analysis areas with an odd number of total lattice sites. In this section, we discuss how the choice of  $L$  influences the value of  $O_p$  as well as the extracted phase transition point.

In the MI phase, we show that integer brane parity  $O_p$  is subject to a perimeter-law scaling,  $\log O_p \sim -L$ ; see Fig. 4(c). Evaluated at different parameter regimes of  $J/U$ , with increasing  $L$ , we additionally observe a slight trend towards lower values than expected for a perimeter law. This behavior can be partially attributed to finite-temperature effects, which lead to the formation of uncorrelated individual holes. Uncorrelated holes would lead to an area-law scaling,  $\log O_p \sim -L^2$ , and thus a downward trend that becomes more dominant with increasingly large analysis sizes (due to the perimeter-area scaling) and with decreasing  $J/U$  (due to the reduced probability of finding correlated pairs). Note that this effect also gives rise to a change in the nearest-neighbor parity correlators shown in Fig. 3 (see also Ref. [7]), which in the perturbative regime yields a relative reduction of about  $2(1 - \bar{n}) \sim 6\%$ , where  $\bar{n}$  denotes the average filling in the atomic limit.

Another reason for a reduced brane parity in the MI phase involves the inhomogeneous confining potential from the lattice beams, leading to a coexistence of different phases in the system depending on the local chemical potential [16]. As a consequence, we expect a bias towards a superfluid when including regions of smaller local

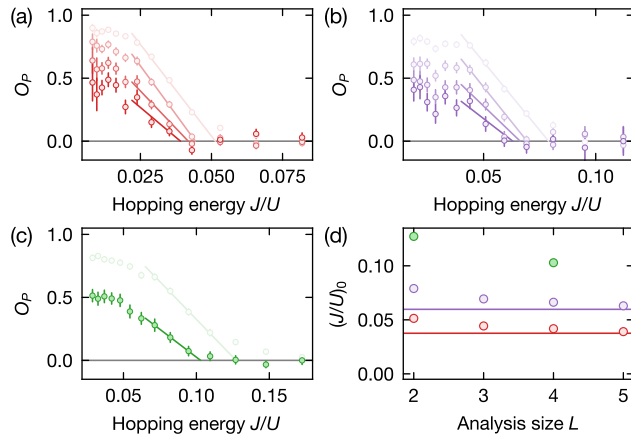


FIG. 9. (a)–(c) Brane parity in the triangular (red), square (purple), and Lieb (green) lattices for increasing analysis sizes (light to dark color), ranging from  $L = 2$ – $5$  for the triangular and square lattice, and  $L = 2, 4$  for the Lieb lattice. The lines indicate linear fits to the sloped  $J/U$ -parameter regime. We extract a simplified estimate for the critical point,  $(J/U)_0$ , as the point where the fit vanishes. Error bars denote the SEM. In panel (d), we show that, with increasing analysis size  $L$ , the extracted phase transition point converges. The horizontal lines indicate the critical value predicted by quantum Monte Carlo simulations.

chemical potential towards the edges of the atomic cloud. As analyzing with larger  $L$  has a higher sampling frequency at the edges than with smaller  $L$ , the inhomogeneity effects are stronger for larger  $L$ .

In the SF phase, one would, in contrast, expect  $\log O_p \sim -L \log L$  scaling [8]. We do not directly observe such scaling since the absolute  $O_p$  values are much smaller and lie within experimental noise already at  $L \sim 4$ . However, due to the difference in scaling compared with the MI phase, we expect integer brane parity to serve as a more accurate proxy for the order parameter when measured on larger analysis areas  $L \times L$ . In Fig. 9, we show the  $J/U$  dependence of  $O_p$  for different  $L$  and extract a simplified estimate for the phase transition point  $(J/U)_0$ : We linearly fit the sloped part of the data (disregarding nonlinear behavior predicted in the immediate vicinity of the phase transition [7,8]) and assign the value at which the fit vanishes as  $(J/U)_0$ , for which we indeed observe convergent behavior for increasing  $L$ .

- [1] M. den Nijs and K. Rommelse, *Preroughening Transitions in Crystal Surfaces and Valence-Bond Phases in Quantum Spin Chains*, *Phys. Rev. B* **40**, 4709 (1989).
- [2] T. Kennedy and H. Tasaki, *Hidden  $Z_2 \times Z_2$  Symmetry Breaking in Haldane-Gap Antiferromagnets*, *Phys. Rev. B* **45**, 304 (1992).
- [3] F. D. M. Haldane, *Nonlinear Field Theory of Large-Spin Heisenberg Antiferromagnets: Semiclassically Quantized*

*Solitons of the One-Dimensional Easy-Axis Néel State*, *Phys. Rev. Lett.* **50**, 1153 (1983).

- [4] E. G. Dalla Torre, E. Berg, and E. Altman, *Hidden Order in 1D Bose Insulators*, *Phys. Rev. Lett.* **97**, 260401 (2006).
- [5] S. de Léséleuc, V. Lienhard, P. Scholl, D. Barredo, S. Weber, N. Lang, H. P. Büchler, T. Lahaye, and A. Browaeys, *Observation of a Symmetry-Protected Topological Phase of Interacting Bosons with Rydberg Atoms*, *Science* **365**, 775 (2019).
- [6] P. Sompert, S. Hirthe, D. Bourgund, T. Chalopin, J. Bibo, J. Koepsell, P. Bojović, R. Verresen, F. Pollmann, G. Salomon, C. Gross, T. A. Hilker, and I. Bloch, *Realizing the Symmetry-Protected Haldane Phase in Fermi–Hubbard Ladders*, *Nature (London)* **606**, 484 (2022).
- [7] M. Endres, M. Cheneau, T. Fukuhara, C. Weitenberg, P. Schauß, C. Gross, L. Mazza, M. C. Bañuls, L. Pollet, I. Bloch, and S. Kuhr, *Observation of Correlated Particle-Hole Pairs and String Order in Low-Dimensional Mott Insulators*, *Science* **334**, 200 (2011).
- [8] S. P. Rath, W. Simeth, M. Endres, and W. Zwerger, *Non-Local Order in Mott Insulators, Duality and Wilson Loops*, *Ann. Phys. (N.Y.)* **334**, 256 (2013).
- [9] T. Hartke, B. Oreg, N. Jia, and M. Zwierlein, *Doublon-Hole Correlations and Fluctuation Thermometry in a Fermi-Hubbard Gas*, *Phys. Rev. Lett.* **125**, 113601 (2020).
- [10] E. Berg, E. G. Dalla Torre, T. Giamarchi, and E. Altman, *Rise and Fall of Hidden String Order of Lattice Bosons*, *Phys. Rev. B* **77**, 245119 (2008).
- [11] C. Degli Esposti Boschi, A. Montorsi, and M. Roncaglia, *Brane Parity Orders in the Insulating State of Hubbard Ladders*, *Phys. Rev. B* **94**, 085119 (2016).
- [12] S. Fazzini, F. Becca, and A. Montorsi, *Nonlocal Parity Order in the Two-Dimensional Mott Insulator*, *Phys. Rev. Lett.* **118**, 157602 (2017).
- [13] C. K. Thomas, T. H. Barter, T.-H. Leung, M. Okano, G.-B. Jo, J. Guzman, I. Kimchi, A. Vishwanath, and D. M. Stamper-Kurn, *Mean-Field Scaling of the Superfluid to Mott Insulator Transition in a 2D Optical Superlattice*, *Phys. Rev. Lett.* **119**, 100402 (2017).
- [14] C. Gross and I. Bloch, *Quantum Simulations with Ultracold Atoms in Optical Lattices*, *Science* **357**, 995 (2017).
- [15] W. S. Bakr, J. I. Gillen, A. Peng, S. Fölling, and M. Greiner, *A Quantum Gas Microscope for Detecting Single Atoms in a Hubbard-Regime Optical Lattice*, *Nature (London)* **462**, 74 (2009).
- [16] J. F. Sherson, C. Weitenberg, M. Endres, M. Cheneau, I. Bloch, and S. Kuhr, *Single-Atom-Resolved Fluorescence Imaging of an Atomic Mott Insulator*, *Nature (London)* **467**, 68 (2010).
- [17] L. Tarruell, D. Greif, T. Uehlinger, G. Jotzu, and T. Esslinger, *Creating, Moving and Merging Dirac Points with a Fermi Gas in a Tunable Honeycomb Lattice*, *Nature (London)* **483**, 302 (2012).
- [18] G.-B. Jo, J. Guzman, C. K. Thomas, P. Hosur, A. Vishwanath, and D. M. Stamper-Kurn, *Ultracold Atoms in a Tunable Optical Kagome Lattice*, *Phys. Rev. Lett.* **108**, 045305 (2012).
- [19] S. Taie, H. Ozawa, T. Ichinose, T. Nishio, S. Nakajima, and Y. Takahashi, *Coherent Driving and Freezing of Bosonic*

- Matter Wave in an Optical Lieb Lattice*, *Sci. Adv.* **1**, e1500854 (2015).
- [20] R. Yamamoto, H. Ozawa, D. C. Nak, I. Nakamura, and T. Fukuhara, *Single-Site-Resolved Imaging of Ultracold Atoms in a Triangular Optical Lattice*, *New J. Phys.* **22**, 123028 (2020).
- [21] J. Yang, L. Liu, J. Mongkolkiattichai, and P. Schauss, *Site-Resolved Imaging of Ultracold Fermions in a Triangular-Lattice Quantum Gas Microscope*, *PRX Quantum* **2**, 020344 (2021).
- [22] D. Barredo, S. de Léséleuc, V. Lienhard, T. Lahaye, and A. Browaeys, *An Atom-by-Atom Assembler of Defect-Free Arbitrary Two-Dimensional Atomic Arrays*, *Science* **354**, 1021 (2016).
- [23] A. M. Kaufman, B. J. Lester, C. M. Reynolds, M. L. Wall, M. Foss-Feig, K. R. A. Hazzard, A. M. Rey, and C. A. Regal, *Two-Particle Quantum Interference in Tunnel-Coupled Optical Tweezers*, *Science* **345**, 306 (2014).
- [24] B. M. Spar, E. Guardado-Sanchez, S. Chi, Z. Z. Yan, and W. S. Bakr, *Realization of a Fermi-Hubbard Optical Tweezer Array*, *Phys. Rev. Lett.* **128**, 223202 (2022).
- [25] D. Greif, T. Uehlinger, G. Jotzu, L. Tarruell, and T. Esslinger, *Short-Range Quantum Magnetism of Ultracold Fermions in an Optical Lattice*, *Science* **340**, 1307 (2013).
- [26] G. Jotzu, M. Messer, R. Desbuquois, M. Lebrat, T. Uehlinger, D. Greif, and T. Esslinger, *Experimental Realization of the Topological Haldane Model with Ultracold Fermions*, *Nature (London)* **515**, 237 (2014).
- [27] M. Xu, L. H. Kendrick, A. Kale, Y. Gang, G. Ji, R. T. Scalettar, M. Lebrat, and M. Greiner, *Doping a Frustrated Fermi-Hubbard Magnet*, [arXiv:2212.13983](https://arxiv.org/abs/2212.13983).
- [28] J. Sebby-Strabley, M. Anderlini, P. S. Jessen, and J. V. Porto, *Lattice of Double Wells for Manipulating Pairs of Cold Atoms*, *Phys. Rev. A* **73**, 033605 (2006).
- [29] C. Weitenberg, M. Endres, J. F. Sherson, M. Cheneau, P. Schauß, T. Fukuhara, I. Bloch, and S. Kuhr, *Single-Spin Addressing in an Atomic Mott Insulator*, *Nature (London)* **471**, 319 (2011).
- [30] T. Fukuhara, A. Kantian, M. Endres, M. Cheneau, P. Schauß, S. Hild, D. Bellem, U. Schollwöck, T. Giamarchi, C. Gross, I. Bloch, and S. Kuhr, *Quantum Dynamics of a Mobile Spin Impurity*, *Nat. Phys.* **9**, 235 (2013).
- [31] P. M. Preiss, R. Ma, M. E. Tai, A. Lukin, M. Rispoli, P. Zupancic, Y. Lahini, R. Islam, and M. Greiner, *Strongly Correlated Quantum Walks in Optical Lattices*, *Science* **347**, 1229 (2015).
- [32] A. W. Young, W. J. Eckner, N. Schine, A. M. Childs, and A. M. Kaufman, *Tweezer-Programmable 2D Quantum Walks in a Hubbard-Regime Lattice*, *Science* **377**, 885 (2022).
- [33] S. Flannigan, L. Madail, R. G. Dias, and A. J. Daley, *Hubbard Models and State Preparation in an Optical Lieb Lattice*, *New J. Phys.* **23**, 083014 (2021).
- [34] M. Rizzi, V. Cataudella, and R. Fazio, *Phase Diagram of the Bose-Hubbard Model with  $T_3$  Symmetry*, *Phys. Rev. B* **73**, 144511 (2006).
- [35] B. Grygiel and K. Patucha, *Excitation Spectra of Strongly Interacting Bosons in the Flat-Band Lieb Lattice*, *Phys. Rev. B* **106**, 224514 (2022).
- [36] B. Capogrosso-Sansone, Ş. G. Söyler, N. Prokof'ev, and B. Svistunov, *Monte Carlo Study of the Two-Dimensional Bose-Hubbard Model*, *Phys. Rev. A* **77**, 015602 (2008).
- [37] N. Teichmann, D. Hinrichs, and M. Holthaus, *Reference Data for Phase Diagrams of Triangular and Hexagonal Bosonic Lattices*, *Europhys. Lett.* **91**, 10004 (2010).
- [38] M. Di Liberto, A. Hemmerich, and C. Morais Smith, *Topological Varma Superfluid in Optical Lattices*, *Phys. Rev. Lett.* **117**, 163001 (2016).
- [39] J. Hur, W. Lee, K. Kwon, S. Huh, G. Y. Cho, and J.-y. Choi, *Measuring Non-Local Brane Order with Error-Corrected Parity Snapshots*, [arXiv:2305.10592](https://arxiv.org/abs/2305.10592).
- [40] U. Bissbort, *Dynamical Effects and Disorder in Ultracold Bosonic Matter*, Ph.D. thesis, Johann Wolfgang Goethe-Universität, Frankfurt (2012).